

The projected future degradation in air quality is caused by more abundant natural aerosols in a warmer world

James Gomez ¹, Robert J. Allen ¹✉, Steven T. Turnock ², Larry W. Horowitz ³, Kostas Tsigaridis ⁴, Susanne E. Bauer⁴, Dirk Olivie⁵, Erik S. Thomson ⁶ & Paul Ginoux³

Previous studies suggest that greenhouse gas-induced warming can lead to increased fine particulate matter concentrations and degraded air quality. However, significant uncertainties remain regarding the sign and magnitude of the response to warming and the underlying mechanisms. Here, we show that thirteen models from the Coupled Model Intercomparison Project Phase 6 all project an increase in global average concentrations of fine particulate matter in response to rising carbon dioxide concentrations, but the range of increase across models is wide. The two main contributors to this increase are increased abundance of dust and secondary organic aerosols via intensified West African monsoon and enhanced emissions of biogenic volatile organic compounds, respectively. Much of the inter-model spread is related to different treatment of biogenic volatile organic compounds. Our results highlight the importance of natural aerosols in degrading air quality under current warming, while also emphasizing that improved understanding of biogenic volatile organic compounds emissions due to climate change is essential for numerically assessing future air quality.

¹Department of Earth and Planetary Sciences, University of California Riverside, Riverside, CA 92521, USA. ²Met Office Hadley Centre, Exeter, UK. ³NOAA/OAR Geophysical Fluid Dynamics Laboratory, Princeton, NJ, USA. ⁴Center for Climate Systems Research, Columbia University, NASA Goddard Institute for Space Studies, New York, NY, USA. ⁵Norwegian Meteorological Institute, Oslo, Norway. ⁶Department of Chemistry and Molecular Biology, Atmospheric Science, University of Gothenburg, Gothenburg, Sweden. ✉email: rjallen@ucr.edu

Air quality is an important aspect of human health¹ and of Sustainable Development Goals involving good health and well-being^{2,3}. Surface-level fine (diameter $\leq 2.5 \mu\text{m}$) particulate matter (PM_{2.5}) is a form of air pollution that is a known carcinogen^{4,5}, is tied to higher infant mortality rates^{6,7}, causes adverse respiratory affects in children⁶, and leads to a worldwide excess mortality rate of 8.8 million per year from all sources, including 5.5 million due to anthropogenic sources and 3.3 due to natural sources⁸.

Owing to multiple interactions involving emissions, chemical processes, deposition and other physical factors (e.g., temperature, precipitation and atmospheric circulation), both the sign and magnitude of PM_{2.5} changes under GHG-induced warming are uncertain^{9–12}. Several studies have emphasized the importance of altered wet removal to increased aerosol burden^{13–16}, through changes in precipitation type (large-scale versus convective) and distribution (e.g., decrease in wet-day frequency). Degraded air quality under warming will likely yield an increase in premature mortality associated with lung cancer and cardiopulmonary disease in most world regions^{17,18}. Such impacts may be exacerbated due to an increased chance of compound extreme events, including concurrent heat waves and air quality extremes^{11,19}.

GHG-induced warming will also impact the emissions of natural aerosols and precursor gases, including biogenic volatile organic compounds (BVOCs), which can oxidize into secondary organic aerosols (SOA). As the production of BVOCs requires carbon obtained from the breakdown of CO₂, BVOC production is tied to photosynthesis^{20,21}. Rising atmospheric CO₂ concentrations are likely to increase the productivity and standing biomass of plants, which allows for an increase in photosynthesis rates²², and thus an increase in the available carbon for BVOC production. An increase in atmospheric CO₂ concentrations, however, can inhibit the production of the BVOC isoprene²³. The biochemical basis for these observations is not fully resolved, but may include CO₂-mediated variations of key substrates such as pyruvate²⁴. Prior modeling studies show that taking this inhibition into account still results in a net increase in isoprene emission, and a relatively large (25%) increase in SOA under future climate change²⁵. Higher atmospheric CO₂ concentrations also promote higher global temperatures, which enhance the enzymatic activities of synthesis that produce isoprene and most other BVOCs^{20,26}. Warming also increases the atmospheric vapor pressure of certain BVOCs surrounding vegetation^{27,28}. As vapor pressure of the BVOCs rise, more can exist in the gaseous phase in the surrounding air, allowing for more oxidation to SOA.

Through altered atmospheric circulation and land change, increasing atmospheric CO₂ concentrations can also influence dust emissions, another important component of PM_{2.5}. The overall response of dust aerosol to climate change, however, remains uncertain. Observations from the Terra and Aqua satellites from 2001–2018 over northern Africa, which is the largest source of dust in the world²⁹, have shown an uncertain response in dust aerosol optical depth (Terra shows a decrease, Aqua an increase), motivating additional analysis³⁰. Longer-term dust depositional records, however, suggest that dust is highly sensitive to climate, with up to a doubling of dust since the preindustrial^{31–33}.

If anthropogenic sources were to be reduced to preindustrial levels ("pristine" air quality), many parts of the world—up to 4.5 billion people—would still be exposed to poor air quality (largely due to dust)³⁴ based on the World Health Organization's (WHO) updated (and more stringent) annual mean PM_{2.5} threshold¹ of $5 \mu\text{g m}^{-3}$. Unlike anthropogenic sources, natural aerosol emissions are highly variable across different regions and not as easily controlled through clean air policies. Moreover, as natural aerosol

emissions are tied to climate (e.g., temperature, winds), continued climate change may have substantial impacts on air quality via altered emissions of natural aerosols and precursor gasses.

Here, we use the most recent state-of-the-art climate and Earth system models, many of which include aerosol and chemistry components that interact with each other and with the biosphere, to quantify the impact of increasing CO₂ on PM_{2.5}-based air quality. Our analysis therefore focuses on CO₂-induced impacts (including temperature, precipitation, etc.) to air quality. We do not address possible reductions of anthropogenic aerosol/precursor gas emissions, which would act to improve air quality. Furthermore, we only address PM_{2.5}-related air quality and do not consider other pollutants such as ozone, which may also respond to climate change. We find a robust increase in PM_{2.5}, largely due to an increase in natural aerosol emissions, including biogenic SOA, dust and sea salt.

Results

Figure 1 shows a spatial map of the multi-model annual mean PM_{2.5} response in years 100–140 from 1% per year CO₂ simulations (relative to the corresponding preindustrial control simulations; Methods) using 13 state-of-the-art CMIP6³⁵ models (Supplementary Tables 1 and 2). In years 100–140, the global annual mean warming is $3.8 \pm 0.4 \text{ K}$. A relatively large and robust signal exists, as the global multi-model annual mean increase is $0.62 \pm 0.26 \mu\text{g m}^{-3}$, or a percent change of $10.8 \pm 3.9\%$ (uncertainties are based on the 90% confidence interval; Methods). All 13 models yield a global mean increase, but with large spread, ranging from $0.001 \mu\text{g m}^{-3}$ in MPI-ESM1-2-HAM (statistically insignificant) to $1.73 \mu\text{g m}^{-3}$ in CESM2-WACCM. Most latitude-longitude grid boxes experience an increase in PM_{2.5}, and model agreement on the increase (Fig. 1b) is generally ~75–85% (significant at the 90% confidence level based on a two-tailed binomial test; Methods). We note that our approximation of PM_{2.5}, and the corresponding response, represents a conservative estimate³⁴ (e.g., climate-dependent changes in fire emissions—which are projected to increase under warming^{36–39}—are not included; Methods).

Figure 1d shows the PM_{2.5} change for each world region (see Fig. 1c for region definitions), and the average over all 12 regions (i.e., global land, abbreviated "Ld" in Fig. 1d). Over global land, the multi-model mean PM_{2.5} increase is $0.83 \pm 0.49 \mu\text{g m}^{-3}$ ($13.7 \pm 6.3\%$). All but one model yields an increase, but again with large inter-model spread ranging from $-0.52 \mu\text{g m}^{-3}$ in MPI-ESM1-2-HAM to $3.1 \mu\text{g m}^{-3}$ in CESM2-WACCM. Ten of the 12 world regions exhibit significant PM_{2.5} increases (the exceptions being Australia at $0.50 \pm 0.51 \mu\text{g m}^{-3}$ and central/north Asia at $0.19 \pm 0.22 \mu\text{g m}^{-3}$), with some regions yielding much larger increases. For example, South America (sAM) experiences the largest PM_{2.5} increase at $2.0 \pm 1.5 \mu\text{g m}^{-3}$ ($42.2 \pm 23.6\%$). Large increases, especially in terms of absolute change, also occur in northern (nAF) and southern (sAF) Africa at $1.7 \pm 1.1 \mu\text{g m}^{-3}$ and $1.3 \pm 1.1 \mu\text{g m}^{-3}$, respectively. The U.S. also experiences large relative increases in PM_{2.5} at $26.6 \pm 13.7\%$.

Although these changes are in response to a large warming signal ($3.8 \pm 0.4 \text{ K}$), we find that PM_{2.5} increases linearly with global mean temperature (Supplementary Note 1; Supplementary Figs. 1 and 2). The real-world evolution of CO₂ is likely to be less aggressive than the 1% per year increase in CO₂ case; as such, the PM_{2.5} increase will likewise be muted relative to that reported here, based on the time of CO₂ quadrupling (years 100–140). Given the linear scaling, however, we expect a 3–4% increase in PM_{2.5} per degree K of warming (this appears unrelated to the rate of warming, as we obtain a similar scaling from the abrupt-4xCO₂ experiments). This estimate is based on CO₂- and vegetation-

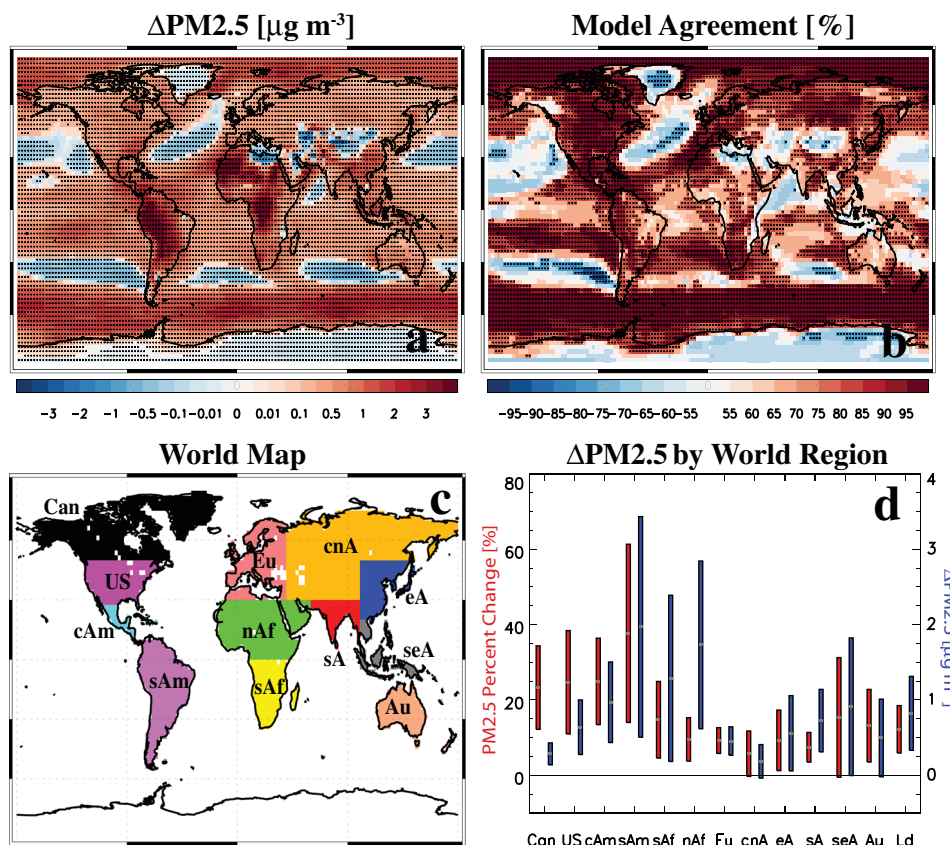


Fig. 1 $PM_{2.5}$ response to GHG-induced warming. **a** Multi-model mean annual mean $PM_{2.5}$ response [$\mu g m^{-3}$]; **b** model agreement on the sign of the $PM_{2.5}$ response [%]; **c** 12 world regions; and **d** absolute [$\mu g m^{-3}$] and relative [%] $PM_{2.5}$ response by world region. Dots in **a** represent a significant response at the 90% confidence level based on a two-tailed pooled *t*-test. Red (blue) colors in **b** indicate model agreement on a $PM_{2.5}$ increase (decrease). Dots in **b** represent a significant model agreement at the 90% confidence level based on a two-tailed binomial test. Bar center (gray horizontal line) in **d** shows the multi-model mean response and bar length represents the 90% confidence interval estimated as $\frac{1.65 \times \sigma}{\sqrt{n_m}}$, where σ is the standard deviation across models and n_m is the number of models. The following abbreviations are used: Canada (Can; black), United States (US; magenta), Central America (cAm; sky blue), South America (sAm; purple), south Africa (sAf; yellow), north Africa (nAf; green), Europe (Eu; pink), central and north Asia (cnA; orange), east Asia (eA; navy), south Asia (sA; red), southeast Asia (seA; gray), and Australia (Au; beige). The average over these 12 land regions is abbreviated as “Ld”.

induced climate change impacts alone, and does not address possible decreases in anthropogenic aerosol/precursor gas emissions (e.g., via clean air policies). Thus, the newest global climate and Earth system models yield a robust $PM_{2.5}$ increase across most world regions under increasing CO_2 concentrations, that linearly scales with the amount of warming.

As with the total $PM_{2.5}$ response, individual $PM_{2.5}$ components also show robust increases over most locations (Supplementary Fig. 3). The largest contributors to the increase in $PM_{2.5}$ over land are organic aerosol (i.e., the sum of primary and secondary organic aerosol; OA $PM_{2.5}$) at 63.7% contribution to the total $PM_{2.5}$ increase; followed by dust (DU $PM_{2.5}$; 26.8%) and sea salt (another natural aerosol) at 6.6%. The other components—sulfate and black carbon—contribute 2.9% and <1% to the increase, respectively. As only two models include nitrate, it is not considered in this analysis (Methods). Furthermore, biomass burning emissions are prescribed in our simulations and thus are not considered further as they are not able to change in response to the increase in CO_2 (Methods). The large contributions of OA $PM_{2.5}$ and DU $PM_{2.5}$ provide an explanation for the larger increase of total $PM_{2.5}$ over the Americas and Africa (Fig. 1; Supplementary Fig. 3). A significant increase in DU $PM_{2.5}$ over both northern (i.e., Sahara Desert) and southern Africa occurs at 1.1 ± 0.9 and $0.19 \pm 0.15 \mu g m^{-3}$ (7.7 ± 6.6 and $22.4 \pm 19.3\%$), respectively. Similarly, an increase in OA $PM_{2.5}$ occurs for both regions at 0.5 ± 0.4 for nAf and $1.0 \pm 0.9 \mu g m^{-3}$ for sAf

(20.4 ± 15.7 and $18.9 \pm 15.4\%$, respectively). Over the US and South America, the relatively large increase in total $PM_{2.5}$ is due to large increases in OA $PM_{2.5}$ at $0.5 \pm 0.3 \mu g m^{-3}$ ($29.4 \pm 19.2\%$) and $1.6 \pm 1.4 \mu g m^{-3}$ ($51.9 \pm 32.8\%$), respectively. Although not significant, DU $PM_{2.5}$ also contributes to the US increase at $0.10 \pm 0.13 \mu g m^{-3}$, and in particular for the relative increase at $42.8 \pm 38.8\%$. Similarly large relative DU $PM_{2.5}$ increases also occur for Central America ($71.7 \pm 25.0\%$), Canada ($57.7 \pm 39.0\%$), and South America ($36.2 \pm 16.2\%$). Much of this DU $PM_{2.5}$ increase over the Americas appears to be transported Saharan dust (e.g., Supplementary Fig. 3c). We note that although the increase in SS $PM_{2.5}$ is the third most important contributor to the increase in $PM_{2.5}$ over global land (which is most important for human-relevant air quality) with a percent increase of $11.6 \pm 5.0\%$, the increase in SS $PM_{2.5}$ becomes more important when considering the global mean (Supplementary Fig. 4; Supplementary Note 2).

Of the 13 models, five (UKESM1-0-LL, NorESM2-LM, GFDL-ESM4, GISS-E2-1-G and CESM2-WACCM) include climate-dependent emissions of BVOCs (Supplementary Table 2; additional discussion below), including monoterpenes and isoprene, which can be oxidized to form SOA. Figure 2a, c shows the $PM_{2.5}$ response in the five models with climate-dependent BVOC emissions (BVOC models) and the eight models without climate-dependent BVOC emissions (NOBVOC models; Supplementary Fig. 5 shows model agreement on the sign of the response). The

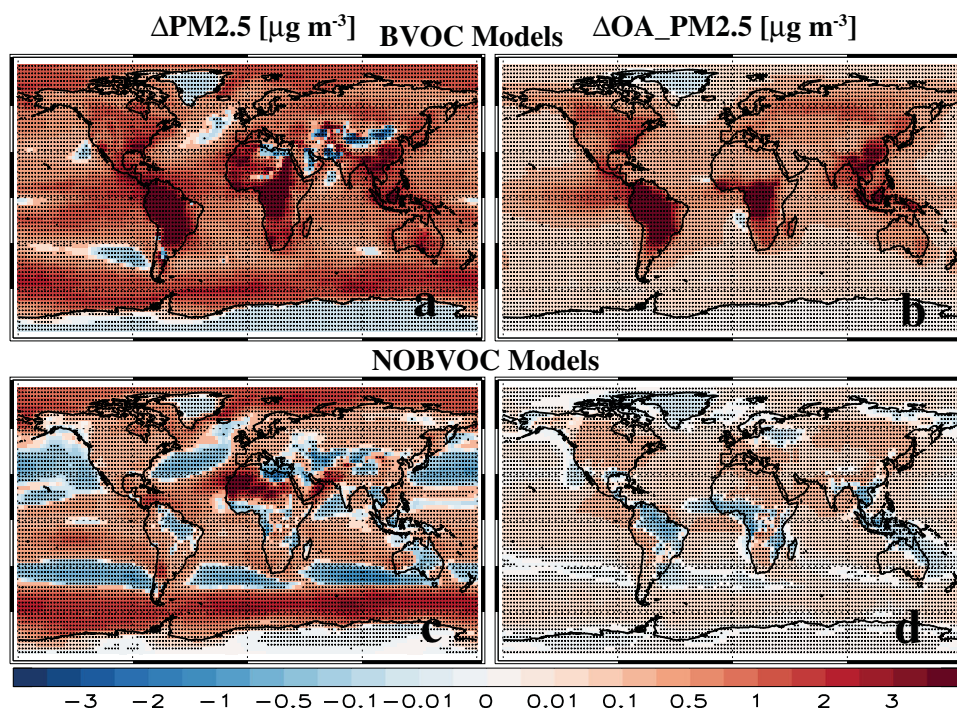


Fig. 2 $PM_{2.5}$ response to GHG-induced warming and the contribution from organic aerosol in two model subsets. Multi-model mean annual mean **a** $PM_{2.5}$ and **b** OA $PM_{2.5}$ response [$\mu g m^{-3}$] in five models with climate-dependent BVOC emissions (BVOC models); and **c**, **d** the corresponding response in eight models that lack climate-dependent BVOC emissions (NOBVOC models). Dots represent a significant response at the 90% confidence level based on a two-tailed pooled *t*-test.

multi-model annual mean increase over land for the BVOC models is $1.7 \pm 0.9 \mu g m^{-3}$ ($23.0 \pm 11.0\%$); the corresponding increase for the NOBVOC models is much smaller at $0.28 \pm 0.27 \mu g m^{-3}$ ($5.4 \pm 5.2\%$). Thus, BVOC models yield a much larger (5–6 times) increase in $PM_{2.5}$ —this accounts for much of the inter-model spread previously discussed. Nearly all of the enhanced $PM_{2.5}$ response is due to OA $PM_{2.5}$ (and more specifically SOA $PM_{2.5}$), particularly over South America and central Africa, as well as east and southeast Asia (Fig. 2b, d). The multi-model annual mean OA $PM_{2.5}$ increase over land for the BVOC models is $1.4 \pm 0.8 \mu g m^{-3}$ ($66.3 \pm 36.9\%$); the corresponding increase for the NOBVOC models is much smaller and not significant at $0.003 \pm 0.05 \mu g m^{-3}$ ($0.17 \pm 2.4\%$). Thus, consistent with prior studies^{25,40,41}, models with climate-dependent BVOC emissions simulate larger increases in OA $PM_{2.5}$, and in turn, larger and more robust increases in $PM_{2.5}$.

We note that the magnitude of the global mean $PM_{2.5}$ increase found here—particularly based on the BVOC models—is comparable to the corresponding end-of-the twenty-first century decrease in $PM_{2.5}$ under near-term climate forcer (NTCF; aerosols and precursor gases) mitigation^{42,43}. Comparing twenty-first century simulations in five climate models (including several used here) driven by SSP3-7.0 (a future emission scenario that lacks climate policy and has weak levels of air quality control measures) relative to SSP3-7.0-lowNTCF (an analogous future emission scenario but with strong levels of air quality control measures), the decrease in global mean $PM_{2.5}$ by 2090–2099 relative to 2005–2014 is $-0.93 \pm 0.07 \mu g m^{-3}$ ³⁴. Here, in this analysis, we find global mean $PM_{2.5}$ increases of $0.62 \pm 0.26 \mu g m^{-3}$, which increases to $1.06 \pm 0.49 \mu g m^{-3}$ in BVOC models. Thus, we find that CO_2 -caused degradation of air quality—under relatively large global mean warming of $3.8 \pm 0.4 K$ (which is similar to end-of-century warming under SSP3-7.0)—is comparable to improvements in air quality due to strong air quality control measures (i.e., NTCF mitigation).

Mechanisms of increased Sahara Dust. The main location of the DU $PM_{2.5}$ increase is over the Sahara Desert and northern Africa (Supplementary Fig. 3c, d). The multi-model annual mean DU $PM_{2.5}$ increase over the region is $1.1 \pm 0.9 \mu g m^{-3}$, with 10 of 13 models (77%) yielding an increase. The largest increase occurs during Northern Hemisphere wintertime (January–February–March, JFM), but this is not significant at $1.5 \pm 1.9 \mu g m^{-3}$. As summertime (July–August–September, JAS) also yields a large (and significant) increase at $1.3 \pm 0.9 \mu g m^{-3}$, we focus on the annual and JAS responses. Figure 3a, b shows the corresponding change in annual and JAS dust emissions (Supplementary Fig. 6 shows model agreement on the sign of the change). Significant increases occur throughout the Sahara region, particularly the western Sahara during JAS. The multi-model annual mean increase over the entire nAF region is $17.3 \pm 17.6 kg km^{-2} day^{-1}$, with 10 of 13 models (77%) yielding an overall increase. Larger (and significant) increases occur during JAS at $38.8 \pm 27.4 kg km^{-2} day^{-1}$ with 77% model agreement. Furthermore, the spatial correlation over nAF between the multi-model mean change in dust emissions and DU $PM_{2.5}$ is 0.79 for the annual mean and 0.84 for JAS (both significant at the 99% confidence level). Thus, the increase in nAF DU $PM_{2.5}$ is related to increased dust emissions. We note both wet and dry dust removal increase over nAF (Supplementary Fig. 7). As this is likely related to increased dust emissions, we also analyze the wet and dry dust removal efficiencies, and find that a decrease in wet removal efficiency also contributes to the increase in dust and other aerosol species (Supplementary Note 3; Supplementary Figs. 8 and 9).

What causes the increase in northern Africa dust emissions? All 13 models used here parameterize dust emissions based (in part) on surface winds (Supplementary Table 2; see also ref. 44), but the degree of coupling to land surface properties and vegetation varies. For example, land cover change impacts dust emissions in GFDL-ESM4, but soil moisture is not directly

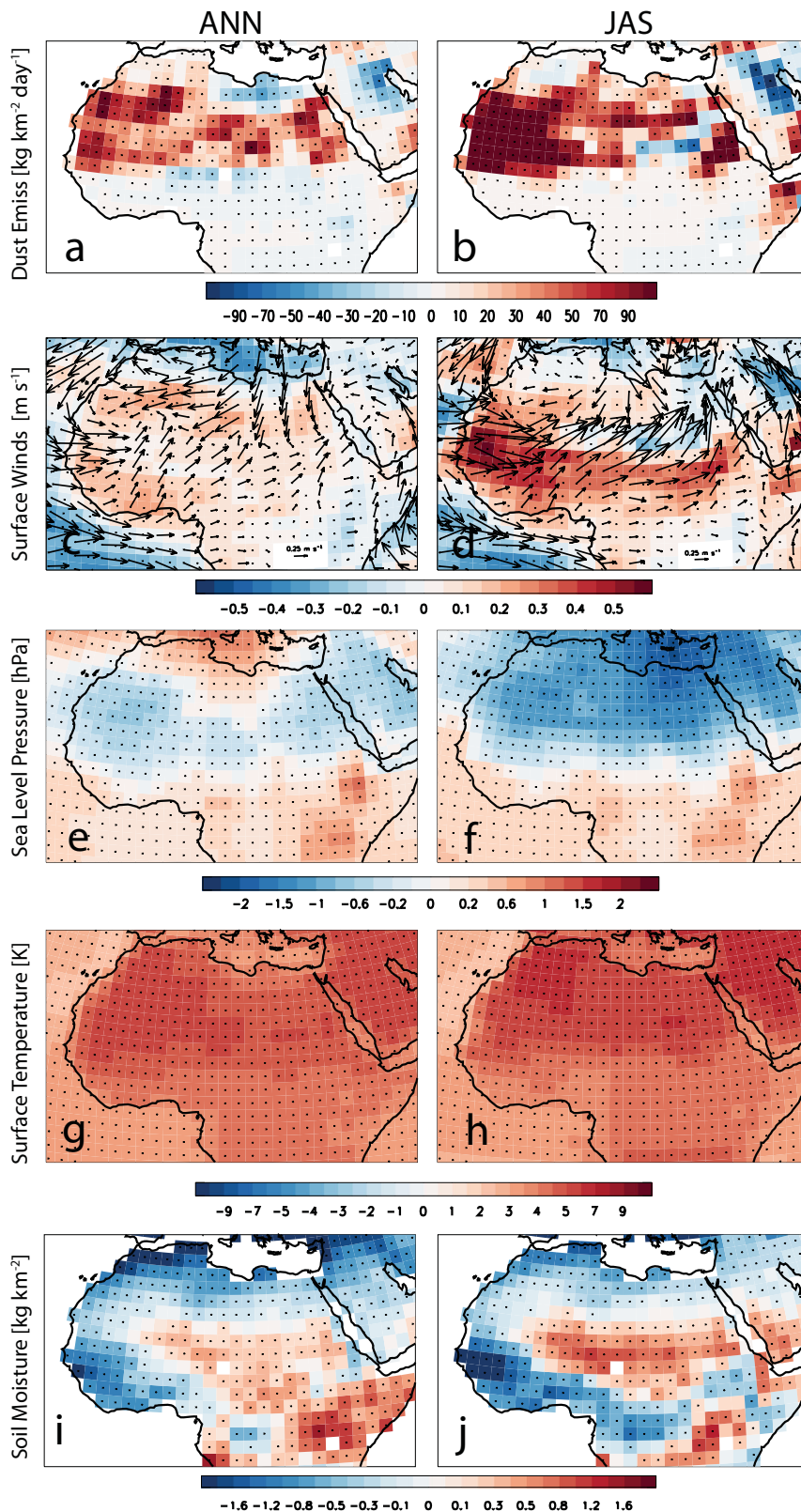


Fig. 3 Response of dust emissions and atmospheric circulation to GHG-induced warming over Africa. Multi-model mean annual mean change in **a** dust emissions [$\text{kg km}^{-2} \text{day}^{-1}$]; **c** surface wind vectors and wind speed [m s^{-1}]; **e** sea level pressure [hPa]; **g** surface temperature [K]; and **i** surface soil moisture [kg km^{-2}]. Corresponding multi-model mean July–August–September (JAS) responses for **b** dust emissions [$\text{kg km}^{-2} \text{day}^{-1}$]; **d** surface wind vectors and wind speed [m s^{-1}]; **f** sea level pressure [hPa]; **h** surface temperature [K]; and **j** surface soil moisture [kg km^{-2}]. Dots represent a significant response at the 90% confidence level based on a two-tailed pooled *t*-test.

used⁴⁵. In GISS-E2-1-G, dust emissions are impacted by irrigation (and soil moisture), but not vegetation^{46,47}. In contrast, CESM2-WACCM uses vegetation, as well as soil moisture, to simulate dust emissions⁴⁸. NorESM2-LM uses a fixed map of soil erodibility and clay content, but includes interactive vegetation (and soil moisture) effects on dust emissions, such as leaf area index and canopy height⁴⁹. UKESM1-0-LL also includes the effects of interactive vegetation on dust emissions, and a prior analysis showed good agreement between UKESM1-0-LL simulated and observed dust changes⁵⁰.

Figure 3c, d shows a multi-model mean increase in surface wind speed throughout most of the region, with enhanced westerly/southwesterly flow, particularly during JAS (Supplementary Fig. 6 shows model agreement). Over the entire region, the multi-model annual mean surface wind speed increase is $0.07 \pm 0.05 \text{ m s}^{-1}$, with 10 of 13 (77%) models yielding an increase. As with most of the responses discussed in this section, the increase in surface wind speed is larger ($0.16 \pm 0.05 \text{ m s}^{-1}$) and more robust (92% model agreement on the increase) during JAS. Figure 3e, f shows a multi-model mean decrease in sea level pressure exists over most of the Sahara region. This strengthens the climatological pressure gradient (i.e., the Sahara is dominated by relatively low sea level pressure, especially during JAS), which is consistent with the enhanced surface winds. The decrease in sea level pressure is related to enhanced surface warming (Fig. 3g, h) —the spatial correlation over nAF between the multi-model mean changes in sea level pressure and surface temperature is -0.68 for the annual mean and -0.87 for JAS (both significant at the 99% confidence level). Consistent with these dynamical changes, there are also significant increases in precipitation throughout most of northern Africa at $0.12 \pm 0.06 \text{ mm day}^{-1}$ ($8.5 \pm 4.6\%$) and $0.27 \pm 0.17 \text{ mm day}^{-1}$ ($10.7 \pm 6.2\%$) for the annual and summertime (Supplementary Fig. 7) mean, with 10 of 13 (77%) models yielding an increase for both seasons. Changes in surface soil moisture are less robust and not significant, likely due to the offsetting effects of warming and increased evaporative demand, relative to the increase in precipitation. For example, nAF annual mean surface soil moisture decreases by $-0.08 \pm 0.19 \text{ kg m}^{-2}$ (6 of 12 models agree on the decrease); during JAS, the decrease is $-0.11 \pm 0.24 \text{ kg m}^{-2}$ (8 of 12 models agree on the decrease). Overall, however, these changes suggest increasing CO_2 drives an enhanced West African Monsoon, which is characterized by northward migration of the tropical rain band during the summer months, and strong southwesterly flow from the south.

Figure 4 shows a scatter plot of the nAF annual mean change in dust emissions versus the corresponding change in near-surface wind speed for each model. With a correlation of 0.57 (significant at the 95% confidence level), models that simulate a larger increase in nAF surface wind speeds also tend to yield a larger increase in nAF dust emissions (and vice versa). The corresponding JAS correlation is 0.50, significant at the 90% confidence level. Another way of quantifying this relationship is by calculating the spatial correlation coefficient (over nAF) between the multi-model mean change in dust emissions and surface wind speed. This approach also yields significant (at the 99% confidence level) correlations, at 0.55 for the annual mean and 0.63 for JAS. Other climate parameters related to dust emissions show weaker correlations (see also Supplementary Note 4). For example, although consistent with expectations (i.e., drier soil is more easily mobilized) the inter-model correlation between the change in nAF surface soil moisture and dust emissions is -0.50 and -0.20 for the annual and summertime mean (the latter correlation is not significant at the 90% confidence level). The corresponding spatial correlation between the multi-model mean change in nAF dust emissions and surface soil moisture is also weak (and not significant) at -0.08 and -0.01 for the annual and

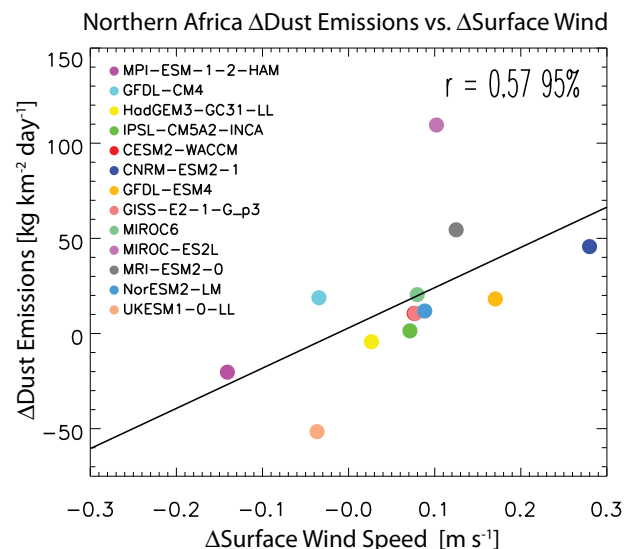


Fig. 4 Change in dust emissions versus the change in surface wind speed over northern Africa in individual models. Scatter plot of the change in dust emissions [$\text{kg km}^{-2} \text{ day}^{-1}$] versus the change in surface wind speed [m s^{-1}] over northern Africa for each model (color coded as defined in the legend). Black line shows the least squares regression slope. The correlation coefficient (r) is 0.57, significant at the 95% confidence level.

summertime mean. This is consistent with visual interpretation, which shows a relatively large decrease in soil moisture in western nAF (Fig. 3i, j), near Nigeria and moving west through Ghana, Ivory Coast, Sierra Leone and Guinea. The bulk of the increase in dust emissions (Fig. 3a, b), however, is to the north of this (where there are also strong increases in surface winds). Furthermore, in northern Africa (e.g., Algeria, Libya, Egypt), there are general decreases in soil moisture but mixed changes in dust emissions (for the annual mean, there are decreased dust emissions near Libya; Fig. 3a). Thus, we conclude that the bulk of the increase in nAF dust emissions is associated with the increase in near-surface wind speeds. The importance of surface winds is consistent with prior studies^{51,52}, including a recent analysis of historical CMIP6 prescribed sea surface temperature (SST) experiments ("AMIP"; SSTs do vary but not interactively) that showed changes in surface winds were the primary driver of changes in dust emissions⁴⁴.

Mechanisms of increased organic aerosol. As mentioned above, models with climate-dependent BVOC emissions yield larger increases in $\text{PM}_{2.5}$, mostly due to larger increases in OA $\text{PM}_{2.5}$ (and in particular SOA). The relatively large increase in OA $\text{PM}_{2.5}$ in these models is consistent with enhanced BVOC emissions (Supplementary Fig. 10). GISS-E2-1-G, however, is an exception, as it yields strong increases in BVOC emissions but a weak increase in OA $\text{PM}_{2.5}$. The OA $\text{PM}_{2.5}$ increase over global land is $2.7, 0.9, 0.01, 2.2,$ and $1.0 \mu\text{g m}^{-3}$ (125.8%, 42.5%, 0.9%, 95% and 35.8%) for CESM2-WACCM, GFDL-ESM4, GISS-E2-1-G, NorESM2-LM and UKESM1-0-LL, respectively.

CMIP6 models use relatively simplistic parameterizations for BVOC emissions, with some models' BVOC emissions dependent on the climate (e.g., temperature; Supplementary Table 2). BVOC-SOA treatment also varies between the models^{53,54}. For example, three of the five BVOC models parameterize SOA formation as a fixed yield from BVOC emissions. UKESM1-0-LL has a fixed SOA yield of 26% from gas-phase oxidation reactions involving interactive land-based monoterpene emissions from a dynamic vegetation and land surface model^{55,56}. NorESM2-LM

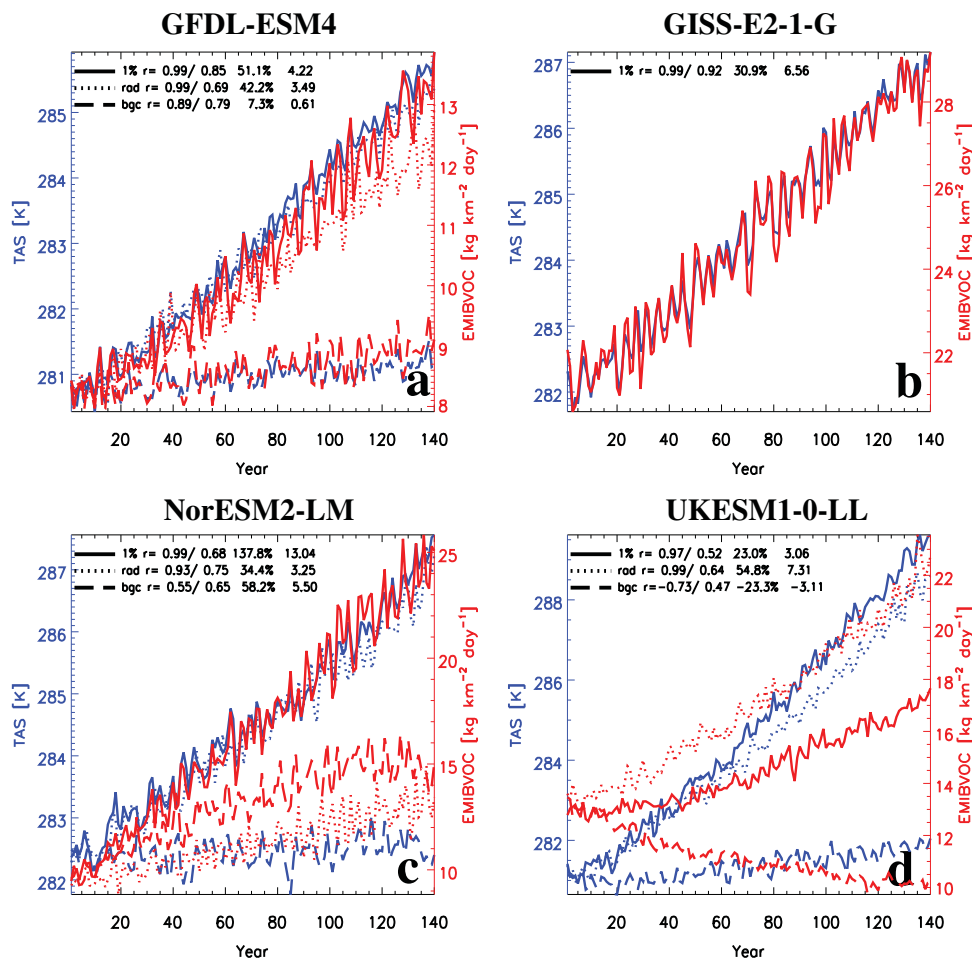


Fig. 5 Global land mean time series of surface temperature and BVOC emissions. Surface temperature (TAS; blue) [K] and BVOC emissions (EMIBVOC; red) [$\text{kg km}^{-2} \text{day}^{-1}$] for four models that include climate-dependent BVOC emissions, including **a** GFDL-ESM4; **b** GISS-E2-1-G; **c** NorESM2-LM; and **d** UKESM1-0-LL. Solid, dotted and dashed lines show results from the 1% per year CO_2 , 1% per year CO_2 -rad, and 1% per year CO_2 -bgc experiments (only three models, GFDL-ESM4, NorESM2-LM and UKESM1-0-LL, performed the latter two experiments). Also included is the correlation coefficient (r), followed by the detrended correlation, the percent change and the absolute change in BVOC emissions (years 100–140 relative to 40 years from the preindustrial control).

has fixed SOA yields of 15% and 5% from oxidation of monoterpenes and isoprene emissions from dynamically evolving vegetation^{40,49,57}. GFDL-ESM4 has a fixed SOA yield of 10% from isoprene and terpene emissions from static present-day vegetation conditions⁵⁸. In contrast, GISS-E2-1-G (OMA; Supplementary Note 5) includes gas-particle partitioning of semi-volatile species (they are able to condense on and evaporate from pre-existing aerosols) that form SOA^{47,53}. Emissions of isoprene from dynamically evolving vegetation are calculated interactively, whereas terpene emissions are prescribed. CESM2-WACCM also explicitly calculates SOA using the volatility basis set (VBS), where aromatic species including terpenes and isoprene (from dynamically evolving vegetation) are oxidized to produce a range of gas-phase SOA precursors with different volatilities^{59,60}.

The strong BVOC increase in GISS-E2-1-G, but relatively weak increase in OA $\text{PM}_{2.5}$ suggests weak SOA formation from the oxidation of BVOCs. This finding is consistent with a prior GISS ModelE2 study⁵³, where SOA was mostly affected by the pre-existing non-volatile primary OA (POA), as opposed to the strong increase in BVOC emissions. Although available in only two models, weak SOA formation in GISS-E2-1-G is supported by the change in chemical SOA production (Supplementary Fig. 11). In GFDL-ESM4 (which experiences relatively large increases in both

BVOC emissions and OA $\text{PM}_{2.5}$), chemical SOA production increases by $0.63 \text{ kg km}^{-2} \text{day}^{-1}$ (49.6%); the corresponding increase in GISS-E2-1-G is much weaker at $0.003 \text{ kg km}^{-2} \text{day}^{-1}$ (8.1%). The GISS-E2-1-G result highlights the possible role of pre-existing aerosols on SOA formation—under the assumption that SOA is able to evaporate under favorable conditions. We note that the 1% per year CO_2 simulations were all conducted with preindustrial anthropogenic aerosols (i.e., low pre-existing aerosol). In addition, other anthropogenic pollution such as nitrogen oxides (NO_x) impact SOA yield from BVOCs⁶¹.

The good correspondence between the change in BVOC emissions and OA $\text{PM}_{2.5}$ (except in GISS-E2-1-G) is also exhibited by their spatial correlation over global land—the correlation is 0.69, 0.89, 0.91, and 0.15 for UKESM1-0-LL, NorESM2-LM, GFDL-ESM4, and GISS-E2-1-G, respectively (all are significant at the 99% confidence level due to the large number of data points). Similar results exist based on the global land time series (over years 1–140) for each model (Supplementary Fig. 12). Here, the correlations (over time) are even stronger for most models at 1.0 for GFDL-ESM4 and NorESM2-LM; 0.97 for UKESM1-0-LL; but 0.27 for GISS-E2-1-G. Detrended correlations are weaker, but still significant at the 90% confidence level outside of GISS-E2-1-G. Thus, the increase in BVOC emissions is a dominant driver of the increase in OA $\text{PM}_{2.5}$ in 3 of

the 4 BVOC models. For CESM2-WACCM (which lacks BVOC emissions data), the increase in OA $PM_{2.5}$ is also likely driven by increased BVOC emissions, due to the similarity of the spatial pattern of the increase in OA $PM_{2.5}$ with the other models (e.g., Supplementary Fig. 10).

What causes the increase in BVOC emissions? Warming is expected to increase BVOC emissions^{55,62}, although this has been questioned⁶³. Temperature increases the emission rates of most BVOCs exponentially by enhancing the enzymatic activities of synthesis, by raising the BVOC vapor pressure, and by decreasing the resistance of the diffusion pathway²⁶. Observational support for this relationship is based on synoptic and interannual timescales; the response on climate change timescales, however, is more uncertain. Rising atmospheric CO_2 concentrations are also likely to increase the productivity and standing biomass of plants, which allows for an increase in photosynthesis rates²², and thus an increase in the available carbon for BVOC production. Figure 5 shows time series over years 1–140 of the global land surface temperature versus BVOC emissions in the 1% per year CO_2 simulations for the four BVOC models that archived the data. As previously discussed, BVOC emissions increase in all four models, with the largest increase in NorESM2-LM at $13.0 \text{ kg km}^{-2} \text{ day}^{-1}$ (137.8%) and the weakest increase in UKESM1-0-LL at $3.1 \text{ kg km}^{-2} \text{ day}^{-1}$ (23%). There is also a very strong correlation between surface temperature and BVOC emissions. In GFDL-ESM4, GISS-E2-1-G and NorESM2-LM, the correlation is 0.99 (0.68–0.92 using detrended values), all significant at the 99% confidence level. The relationship is also significant in UKESM1-0-LL, but somewhat weaker with a correlation of 0.97 (0.52 using detrended values). This shows the importance of surface warming to the increase in BVOC emissions, and also supports the linear scaling of warming with changes in $PM_{2.5}$ (e.g., Supplementary Note 1; Supplementary Fig. 1).

Three of the five BVOC models—GFDL-ESM4, NorESM2-LM and UKESM1-0-LL—also conducted 1% per year CO_2 -rad (radiatively coupled) and 1% per year CO_2 -bgc (biogeochemically coupled) simulations (Methods). In the former, the increase in CO_2 only impacts the physical climate via radiation; in the latter, the increase in CO_2 only impacts biogeochemical processes⁶⁴. In the context of BVOC emissions, the 1% per year CO_2 -rad experiments largely isolate the temperature and precipitation impacts; the 1% per year CO_2 -bgc experiments isolate the increased biomass productivity (i.e., CO_2 fertilization effects, and the CO_2 isoprene suppression effects for models that include it). In NorESM2-LM, global land BVOC emissions increase under both 1% per year CO_2 -rad ($3.3 \text{ kg km}^{-2} \text{ day}^{-1}$; 34.4%) and 1% per year CO_2 -bgc ($5.5 \text{ kg km}^{-2} \text{ day}^{-1}$; 58.2%). GFDL-ESM4 also yields an increase in BVOC emissions under both experiments, largely under 1% per year CO_2 -rad ($3.5 \text{ kg km}^{-2} \text{ day}^{-1}$; 42.2%), with smaller increases under 1% per year CO_2 -bgc ($0.61 \text{ kg km}^{-2} \text{ day}^{-1}$; 7.3%). In UKESM1-0-LL, BVOC emissions also (strongly) increase under 1% per year CO_2 -rad ($7.3 \text{ kg km}^{-2} \text{ day}^{-1}$; 54.8%), but decrease under 1% per year CO_2 -bgc ($-3.1 \text{ kg km}^{-2} \text{ day}^{-1}$; -23.3%).

Thus, all three models simulate an increase in BVOC emissions in response to CO_2 -induced changes in the physical climate (i.e., warming). The magnitude of the increase, however, varies by more than a factor of 2; the stronger increase in UKESM1-0-LL suggests this model's BVOC emissions are more sensitive to warming than the other two models. In response to CO_2 -induced changes in biogeochemistry, models simulate different signed responses. The UKESM1-0-LL decrease in BVOC emissions under 1% per year CO_2 -bgc is consistent with its strong inhibition of isoprene emissions (Supplementary Note 6; Supplementary Fig. 13) under increasing CO_2 concentrations^{23,55}. Although NorESM2-LM also includes this effect (Supplementary Table 2)

the strong BVOC (and isoprene) increase in NorESM2-LM (and also likely CESM2-WACCM) implies weak isoprene inhibition and/or compensating effects. For example, all BVOC models except GISS-E2-1-G yield increases in leaf area index (LAI) (and net primary productivity of land biomass, NPP) in both 1% per year CO_2 and 1% per year CO_2 -bgc (the increase is largely due to biogeochemical CO_2 effects). In models where dynamic vegetation influences BVOC emissions (not GFDL-ESM4), this likely leads to increased isoprene emissions⁶². The increase in LAI and NPP under 1% per year CO_2 is also robust over a larger number (ten) of models (Supplementary Fig. 14), where the global land increase is 0.82 ± 0.29 ($50.7 \pm 19.7\%$) for LAI and $721.7 \pm 101.1 \text{ kg C km}^{-2} \text{ day}^{-1}$ ($80.7 \pm 11.2\%$). All world regions experience an increase in both quantities under the multi-model mean.

Discussion

Our results show that improved understanding of climate-dependent BVOC emissions—including the response to increasing temperature and carbon dioxide (CO_2), as well as the formation of SOA from BVOCs⁶⁵—is critical to numerical assessments of future air quality, and for reducing the uncertainty in the magnitude of the $PM_{2.5}$ increase under climate change. Earth system model development should focus on these types of processes and feedbacks (i.e., chemistry-climate-biosphere) to represent more comprehensive CO_2 -induced impacts on air quality (and climate). Although our experiments are idealized (i.e., 1% per year CO_2), uncertainties exist, and we do not address possible reductions of anthropogenic aerosol/precursor gas emissions, this study emphasizes an increased importance of natural aerosols to air quality under warming. This “climate penalty” will impact a region's ability to attain a specified air quality standard. In fact, CO_2 -caused degradation of air quality—under relatively large global mean warming of $3.8 \pm 0.4 \text{ K}$ (which is similar to end-of-century warming under SSP3-7.0)—is comparable to 21st century improvements in air quality due to strong air quality control measures (i.e., NTCF mitigation)^{42,43}. For a future with clean air, it is thus imperative to decrease CO_2 (and other GHG) emissions.

Methods

CMIP6 simulations. We use 13 state-of-the-art CMIP6 climate models (Supplementary Tables 1 and 2). Our primary analysis focuses on the fully coupled 1% per year CO_2 simulations, where atmospheric CO_2 concentrations increase from the preindustrial value ($\sim 284 \text{ ppm}$) by 1% per year. Both biogeochemical and radiative processes respond to the increasing atmospheric CO_2 concentrations. These experiments are integrated for 140–150 years. Based on a ~ 70 year doubling time, this implies atmospheric CO_2 concentrations have doubled by year 70 and quadrupled near the end of the simulation in year 140.

Preindustrial control and 1% per year CO_2 experiments have natural and anthropogenic emissions (including agriculture and wildfire emissions). Anthropogenic emissions are prescribed based on year 1850 of the CMIP6 emission inventory, the Community Emissions Data System (CEDS)^{35,66}. CMIP6 models, and more specifically the experiments analyzed here including the preindustrial control and 1% per year CO_2 , do not include interactive wildfire OA/BC emissions (i.e., those that respond to climate change). Both sets of simulations therefore include anthropogenic and biomass burning emissions, but they are unchanging on interannual times scales (they do have seasonal variation). Natural aerosol emissions are parameterized based on simulated climate parameters (e.g., surface winds for dust emissions; Supplementary Table 2). Most models include a representation of BVOC emissions from vegetation. Even with some of the NOBVOC models, BVOC emissions exist but they are prescribed (Supplementary Table 2). For example, MIROC6 uses prescribed (interannually fixed and unable to respond to CO_2 increases) isoprene and terpene emissions from the Global Emissions Initiative (GEIA). In BVOC models, BVOC emissions respond to climate change (e.g., changes in CO_2 , temperature, etc.) and, in most cases, vegetation change too. Dynamically evolving vegetation means that vegetation changes in response to climate change. This will impact BVOC emissions. Thus, anthropogenic emissions are the same in the preindustrial control and 1% per year CO_2 experiments; they are not the cause of any increase in $PM_{2.5}$. CO_2 -induced warming, however, will impact natural aerosol emissions (dust and BVOCs in

BVOC models) in 1% per year CO₂; warming will also impact temperature, clouds, precipitation and circulation—all of which could impact PM_{2.5} via chemistry, removal, transport, etc.

Two sets of additional 1% per year CO₂ simulations were also analyzed for three models, including the biogeochemically (1% per year CO₂-bgc) coupled simulation and the radiatively (1% per year CO₂-rad) coupled simulation. In the former, biogeochemical processes over land and ocean respond to increasing atmospheric CO₂ concentration, but the atmospheric radiative transfer calculations use a CO₂ concentration that remains at the initial, preindustrial value. Although climate change is largely muted in these simulations, small changes do occur in response to changes in latent and sensible heat fluxes resulting from changes in vegetation structure and stomatal closure, as well as changes in vegetation coverage in models with dynamic vegetation⁶⁴. In radiatively coupled simulations, increasing atmospheric CO₂ concentration impacts atmospheric radiative transfer and thus climate, but not the biogeochemical processes directly over land and ocean (which see the preindustrial atmospheric CO₂ concentration). These two sets of simulations are used to better understand the drivers of changes in BVOC emissions (i.e., biogeochemical drivers versus physical climate drivers). Of the five models with climate-dependent BVOC emissions, only three (GFDL-ESM4, NorESM2-LM and UKESM1-0-LL) performed the 1% per year CO₂-rad and 1% per year CO₂-bgc simulations and archived the data relevant to this analysis. In all experiments used, biomass burning emissions of aerosols and precursors are prescribed (i.e., they are not coupled to climate-change induced fire changes).

It should be noted that NorESM2-LM, GFDL-ESM4, and CESM2-WACCM utilize the Model of Emissions of Gases and Aerosols from Nature (MEGAN⁶⁷; Supplementary Table 2), which may in part explain the similarity of the results in these three models (note, however, that GFDL-ESM4 lacks the CO₂-isoprene inhibition). MEGAN BVOC emissions are based on a mechanistic model that includes the major processes driving BVOC emission variations. This includes a light response based on electron transport²⁸, a temperature response based on enzymatic activity²⁸, and a CO₂ response based on changes in metabolite pools, enzyme activity and gene expression⁶⁸. The emission activity factor (γ_i) for each compound class i (e.g., isoprene, β -Pinene, α -Pinene, etc.) accounts for the processes controlling emission responses to environmental and phenological conditions. This includes the emission response to light (γ_P), temperature (γ_T), leaf age (γ_A), soil moisture (γ_{SM}), leaf area index (LAI), and CO₂ inhibition (γ_C), i.e., $\gamma_i = (\text{LAI}) \times (\gamma_{P,i}) \times (\gamma_{T,i}) \times (\gamma_{A,i}) \times (\gamma_{SM,i}) \times (\gamma_{C,i}) \times (C_{CE})$, where C_{CE} is the canopy environment coefficient.

The temperature emission activity factor ($\gamma_{T,i}$) is the weighted average of a light-dependent (LDF) and light-independent fraction (LIF = 1 - LDF) according to: $\gamma_{T,i} = (1 - \text{LDF}_i) \times \gamma_{\text{TLIF},i} + \text{LDF}_i \times \gamma_{\text{TLDf},i}$. The light-dependent fraction response is calculated following: $\gamma_{\text{TLDf},i} = E_{\text{opt}} \times [C_{T2} \times \exp(C_{T1,i} \times x) / (C_{T2} - C_{T1,i} \times (1 - \exp(C_{T2} \times x)))]$, where $x = ((1/T_{\text{opt}}) - (1/T)) / 0.00831$, T is leaf temperature (K), $C_{T1,i}$ and C_{T2} (=230) are empirically determined coefficients, $T_{\text{opt}} = 313 + (0.6 \times (T_{240} - T_3))$ and $E_{\text{opt}} = C_{\text{eo},i} \times \exp(0.05 \times (T_{24} - T_3)) \times \exp(0.05 \times (T_{240} - T_3))$. Here, T_3 represents the standard conditions for leaf temperature (=297 K), T_{24} is the average leaf temperature of the past 24 h, T_{240} is the average leaf temperature of the past 240 h, and $C_{\text{eo},i}$ is an emission-class dependent empirical coefficient⁶⁷. The response of the light-independent fraction follows the monoterpene exponential temperature response function⁶⁹ as $\gamma_{\text{TLIF},i} = \exp(\beta_i \times (T - T_3))$, where β_i is an empirically determined coefficient⁶⁷.

Approximation of PM_{2.5}. Air quality is quantified in terms of fine particulate matter, PM_{2.5}. Few models directly archive PM_{2.5} (for those that do, see Supplementary Notes 7–9 for a comparison to our approximated PM_{2.5}) and not all models include the same aerosol species (e.g., nitrate aerosol)^{42,43}. We therefore use the following PM_{2.5} approximation⁷⁰: $\text{PM}_{2.5} = \text{SO}_4 + \text{OA} + \text{BC} + 0.10 \times \text{DU} + 0.25 \times \text{SS}$, where SO₄ is sulfate aerosol, OA is organic aerosol (the sum of primary and secondary organic aerosol, i.e., POA+SOA), BC is black carbon, DU is dust and SS is sea salt. Monthly mean fields from the model level closest to the surface are used. This formula assumes 100% of the BC, OA, and SO₄ is fine mode, whereas 25% of the sea salt and 10% of the dust is fine mode. The SS and DU factors will be dependent on the model and its size distribution. In the case of CNRM-ESM2-1, sensitivity tests were used to estimate a much smaller SS factor of 0.01. This smaller factor addresses the large SS size range of up to 20 μm in this model⁴². To convert PM_{2.5} from a mass mixing ratio to a concentration (units of $\mu\text{g m}^{-3}$), we multiply by air density, $\frac{\text{PS}}{\text{TAS} \times R_d} \times 10^9$, where PS is surface pressure in Pascals, TAS is surface temperature in Kelvin, and R_d is the dry gas constant equal to 287 J K⁻¹ kg⁻¹. Upon multiplying by any factors (i.e., for SS and DU), and converting to concentration, individual PM_{2.5} components are abbreviated as e.g., OA PM_{2.5} and DU PM_{2.5} for the organic aerosol and dust components, respectively.

Although this approach likely introduces some uncertainties, it provides an estimate of PM_{2.5} for all models, as well as a consistent estimate for all models. It also allows us to decompose the total PM_{2.5} into its individual components. Previous work has shown this approach to be a conservative way of estimating PM_{2.5} from CMIP model output⁴⁴. As previously quantified (using the same PM_{2.5} approximation), CMIP6 models generally underestimate PM_{2.5} over most regions relative to ground-based (e.g., GASSP) observations and the MERRA-2 aerosol reanalysis product^{34,71}. Additional details—including analyses of archived PM_{2.5}, an alternative PM_{2.5} approximation with a larger dust factor (i.e., 0.3 as opposed to

0.1), analysis of nitrate and ammonium in the two models (GFDL-ESM4 and GISS-E2-1-G) that include it, and the likely importance of increased natural fire emissions to degraded air quality under warming (which are not included here)—can be found in Supplementary Notes 7–9 and Supplementary Figs. 15 and 16.

Data processing and statistics. We use monthly mean CMIP6 data and spatially interpolate all model data to a 2.5° × 2.5° grid using bilinear interpolation. The climate response is estimated as the difference in years 100–140 (e.g., from the 1% per year CO₂ experiments) relative to 40 years from the preindustrial control simulation corresponding to years 100–140 of the 1% per year CO₂ experiment. Preindustrial control simulations feature fixed (to the preindustrial value) atmospheric CO₂ concentration and other climate drivers (e.g., other GHGs, solar irradiance, aerosols). The multi-model mean is estimated from the average of each individual model. Only one run for each model and experiment is used.

Statistical significance of the climate response is calculated using two different methods. In the first method (e.g., Fig. 1a), the multi-model mean time series is calculated for both the experiment and the control, and a difference is calculated. A two-tailed pooled t -test is used to assess significance, where the null hypothesis of a zero difference is evaluated, with $n_1 + n_2 - 2$ degrees of freedom, where n_1 and n_2 are the number of years in the experiment and control (i.e., 40 years each). Here, the pooled variance, $\frac{(n_1-1)S_1^2 + (n_2-1)S_2^2}{n_1+n_2-2}$, is used, where S_1 and S_2 are the sample variances. Statistical significance assessed using this method shows that the multi-model mean response at nearly all grid boxes (e.g., Fig. 1a) is significant at the 90% confidence level.

We also quantify the significance of the multi-model mean response relative to each individual model response (e.g., Fig. 1d and quoted throughout the text to quantify global and regional uncertainty). Here, the multi-model mean response is calculated as the average of the individual model responses and its uncertainty is estimated as plus/minus 1.65 × standard error (i.e., the 90% confidence interval) according to $\frac{1.65 \times \sigma}{\sqrt{n_m}}$, where σ is the standard deviation across models and n_m is the number of models. If this confidence interval does not include zero, then the multi-model mean response is significant at the 90% confidence level. This approach shows most world regions yield a significant increase in PM_{2.5} (e.g., Fig. 1d).

We also estimate the model agreement on the sign of the model-mean response (e.g., Fig. 1b), which is estimated at each grid box (or world region) as the percentage of models that yield a positive or negative response. Grid points for which 10 out of 13 models (~75%) agree on sign pass a 2-tailed binomial test to reject the null hypothesis of equal probability of positive or negative sign at the 90% confidence level. Under such conditions, there is good agreement on the sign of the response across the models. This approach shows high model agreement (75–85%) on the sign of the PM_{2.5} response (i.e., an increase) at most grid boxes (e.g., Fig. 1b) and world regions (as discussed in the main text).

Significance of correlations (r) is estimated from a two-tailed t -test as: $t = \frac{r}{\sqrt{\frac{1-r^2}{N-2}}}$, with $N - 2$ degrees of freedom. Here, N is either the number of grid boxes (for a spatial correlation) or the number of years (for a correlation over time).

Data availability

CMIP6 data can be downloaded from the Earth System Grid Federation at <https://esgf-node.llnl.gov/search/cmip6/>.

Code availability

Code used to analyze model data is available upon request from rjallen@ucr.edu.

Received: 1 August 2022; Accepted: 23 January 2023;

Published online: 02 February 2023

References

- World Health Organization. *WHO Global Air Quality Guidelines. Particulate Matter (PM 2.5 and PM 10), Ozone, Nitrogen Dioxide, Sulfur Dioxide and Carbon Monoxide* (World Health Organization, 2021).
- Lelieveld, J. Clean air in the Anthropocene. *Faraday Discuss* **200**, 693–703 (2017).
- Amann, M. et al. Reducing global air pollution: the scope for further policy interventions. *Philos. Trans. R. Soc. A: Math. Phys. Eng. Sci.* **378**, 20190331 (2020).
- Ethan, C. J. et al. Association between PM_{2.5} and mortality of stomach and colorectal cancer in Xi'an: a time-series study. *Environ. Sci. Pollut. Res.* **27**, 22353–22363 (2020).
- Huang, F., Pan, B., Wu, J., Chen, E. & Chen, L. Relationship between exposure to PM_{2.5} and lung cancer incidence and mortality: a meta-analysis. *Oncotarget* **8**, 43322–43331 (2017).

6. Bell, M. L., Dominici, F., Ebisu, K., Zeger, S. L. & Samet, J. M. Spatial and temporal variation in PM_{2.5} chemical composition in the United States for health effects studies. *Environ. Health Perspect.* **115**, 989–995 (2007).
7. Jung, E. M. et al. Association between prenatal exposure to PM_{2.5} and the increased risk of specified infant mortality in South Korea. *Environ. Int.* **144**, 105997 (2020).
8. Lelieveld, J. et al. Effects of fossil fuel and total anthropogenic emission removal on public health and climate. *Proc. Natl Acad. Sci. USA* **116**, 7192–7197 (2019).
9. Kirtman, B. et al. Near-term climate change: projections and predictability. In: *Climate Change 2013: The Physical Science Basis. Contribution of Working Group I to the Fifth Assessment Report of the Intergovernmental Panel on Climate Change* (eds Stocker, T.F., D. Qin, G.-K. Plattner, M. Tignor, S.K. Allen, J. Boschung, A. Nauels, Y. Xia, V. Bex and P.M. Midgley). Tech. Rep. 953–1028 (Cambridge University Press, 2013).
10. Westervelt, D. et al. Quantifying PM_{2.5}-meteorology sensitivities in a global climate model. *Atmospheric Environment* **142**, 43–56 (2016).
11. Szopa, S. et al. In *Short-Lived Climate Forcers* (eds Masson-Delmotte, V. et al.) *Climate Change 2021: The Physical Science Basis. Contribution of Working Group I to the Sixth Assessment Report of the Intergovernmental Panel on Climate Change*. 817–922 (Cambridge University Press, 2021).
12. Doherty, R. M., O'Connor, F. M. & Turnock, S. T. Projections of future air quality are uncertain. But which source of uncertainty is most important? *J. Geophys. Res. Atmos.* **127**, e2022JD037948 (2022).
13. Allen, R. J., Landuyt, W. & Rumbold, S. T. An increase in aerosol burden and radiative effects in a warmer world. *Nat. Clim. Chang* **6**, 269–274 (2016).
14. Xu, Y. & Lamarque, J. Isolating the meteorological impact of 21st century GHG warming on the removal and atmospheric loading of anthropogenic fine particulate matter pollution at global scale. *Earth's Future* **6**, 428–440 (2018).
15. Allen, R. J., Hassan, T., Randles, C. A. & Su, H. Enhanced land–sea warming contrast elevates aerosol pollution in a warmer world. *Nat. Clim. Chang* **9**, 300–305 (2019).
16. Banks, A., Kooperman, G. J. & Xu, Y. Meteorological influences on anthropogenic PM_{2.5} in future climates: species level analysis in the community earth system model v2. *Earth's Future* **10**, e2021EF002298 (2022).
17. Silva, R. A. et al. Future global mortality from changes in air pollution attributable to climate change. *Nat. Clim. Chang* **7**, 647–651 (2017).
18. Park, S., Allen, R. J. & Lim, C. H. A likely increase in fine particulate matter and premature mortality under future climate change. *Air Qual. Atmos. Health* **13**, 143–151 (2020).
19. Fiore, A. M., Naik, V. & Leibensperger, E. M. Air quality and climate connections. *J Air Waste Manag Assoc* **65**, 645–685 (2015).
20. Sharkey, T. D. & Yeh, S. Isoprene emission from plants. *Annu Rev Plant Physiol Plant Mol Biol.* **52**, 407–436 (2001).
21. Šimpraga, M. et al. Clear link between drought stress, photosynthesis and biogenic volatile organic compounds in *Fagus sylvatica* L. *Atmos. Environ.* **45**, 5254–5259 (2011).
22. Haverd, V. et al. Higher than expected CO₂ fertilization inferred from leaf to global observations. *Glob. Chang. Biol.* **26**, 2390–2402 (2020).
23. Arneth, A. et al. Process-based estimates of terrestrial ecosystem isoprene emissions: incorporating the effects of a direct CO₂-isoprene interaction. *Atmos. Chem. Phys.* **7**, 31–53 (2007).
24. Rosenstiel, T. N., Ebbets, A. L., Khatri, W. C., Fall, R. & Monson, R. K. Induction of poplar leaf nitrate reductase: a test of extrachloroplastic control of isoprene emission rate. *Plant Biol.* **6**, 12–21 (2004).
25. Lin, G., Penner, J. E. & Zhou, C. How will SOA change in the future? *Geophys. Res. Lett.* **43**, 1718–1726 (2016).
26. Peñuelas, J. & Staudt, M. BVOCs and global change. *Trend. Plant Sci.* **15**, 133–144 (2010).
27. Tingey, D. T., Manning, M., Grothaus, L. C. & Burns, W. F. Influence of light and temperature on monoterpene emission rates from slash pine. *Plant Physiol.* **65**, 797–801 (1980).
28. Guenther, A. B., Monson, R. K. & Fall, R. Isoprene and monoterpene emission rate variability: observations with eucalyptus and emission rate algorithm development. *J. Geophys. Res. Atmos.* **96**, 10799–10808 (1991).
29. Middleton, N. J. & Goudie, A. S. Saharan dust: sources and trajectories. *Trans. Inst. Br. Geogr.* **26**, 165–181 (2001).
30. Voss, K. K. & Evan, A. T. A new satellite-based global climatology of dust aerosol optical depth. *J. Appl. Meteorol. Climatol.* **59**, 83–102 (2020).
31. Mahowald, N. M. et al. Observed 20th century desert dust variability: impact on climate and biogeochemistry. *Atmos. Chem. Phys.* **10**, 10875–10893 (2010).
32. Hooper, J. & Marx, S. A global doubling of dust emissions during the Anthropocene? *Glob. Planet. Chang.* **169**, 70–91 (2018).
33. Kok, J. F. et al. The impacts of mineral dust aerosols on global climate and climate change. *Nat. Rev. Earth Environ.* <https://doi.org/10.31233/X5W06R> (in review).
34. Zhao, X., Allen, R. J. & Thomson, E. S. An implicit air quality bias due to the state of pristine aerosol. *Earth's Future* **9**, e2021EF001979 (2021).
35. Eyring, V. et al. Overview of the Coupled Model Intercomparison Project Phase 6 (CMIP6) experimental design and organization. *Geosci. Model Dev.* **9**, 1937–1958 (2016).
36. Yue, X., Mickley, L. J., Logan, J. A. & Kaplan, J. O. Ensemble projections of wildfire activity and carbonaceous aerosol concentrations over the western United States in the mid-21st century. *Atmos. Environ.* **77**, 767–780 (2013).
37. Val Martin, M. et al. How emissions, climate, and land use change will impact mid-century air quality over the United States: a focus on effects at national parks. *Atmos. Chem. Phys.* **15**, 2805–2823 (2015).
38. Neumann, J. E. et al. Estimating PM_{2.5}-related premature mortality and morbidity associated with future wildfire emissions in the western US. *Environ. Res. Lett.* **16**, 035019 (2021).
39. Xie, Y. et al. Tripling of western US particulate pollution from wildfires in a warming climate. *Proc. Natl Acad. Sci. USA* **119**, e2111372119 (2022).
40. Sporre, M. K., Blichner, S. M., Karset, I. H. H., Makkonen, R. & Berntsen, T. K. BVOC-aerosol-climate feedbacks investigated using NorESM. *Atmos. Chem. Phys.* **19**, 4763–4782 (2019).
41. Yli-Juuti, T. et al. Significance of the organic aerosol driven climate feedback in the boreal area. *Nat. Commun.* **12**, 5637 (2021).
42. Allen, R. J. et al. Climate and air quality impacts due to mitigation of non-methane near-term climate forcers. *Atmos. Chem. Phys.* **20**, 9641–9663 (2020).
43. Allen, R. J. et al. Significant climate benefits from near-term climate forcer mitigation in spite of aerosol reductions. *Environ. Res. Lett.* **16**, 034010 (2021).
44. Zhao, A., Ryder, C. L. & Wilcox, L. J. How well do the CMIP6 models simulate dust aerosols? *Atmos. Chem. Phys.* **22**, 2095–2119 (2022).
45. Evans, S., Ginoux, P., Malyshev, S. & Shevliakova, E. Climate-vegetation interaction and amplification of Australian dust variability. *Geophys. Res. Lett.* **43**, 11,823–11,830 (2016).
46. Miller, R. L. et al. Mineral dust aerosols in the NASA Goddard Institute for Space Sciences ModelE atmospheric general circulation model. *J. Geophys. Res. Atmos.* **111**, D06208 (2006).
47. Bauer, S. E. et al. Historical (1850–2014) aerosol evolution and role on climate forcing using the GISS ModelE2.1 contribution to CMIP6. *J. Adv. Model. Earth Syst.* **12**, e2019MS001978 (2020).
48. Albani, S. et al. Improved dust representation in the community atmosphere model. *J. Adv. Model. Earth Syst.* **6**, 541–570 (2014).
49. Kirkevåg, A. et al. A production-tagged aerosol module for Earth system models, OsloAero5.3—extensions and updates for CAM5.3-Oslo. *Geosci. Model Dev.* **11**, 3945–3982 (2018).
50. Woodward, S. et al. The simulation of mineral dust in the United Kingdom Earth System Model UKESM1. *Atmos. Chem. Phys. Discussions* **22**, 14503–14528 (2022).
51. Evan, A. T. Surface winds and dust biases in climate models. *Geophys. Res. Lett.* **45**, 1079–1085 (2018).
52. Pu, B. & Ginoux, P. How reliable are CMIP5 models in simulating dust optical depth? *Atmos. Chem. Phys.* **18**, 12491–12510 (2018).
53. Tsigaridis, K. & Kanakidou, M. The present and future of secondary organic aerosol direct forcing on climate. *Curr. Clim. Chang. Rep.* **4**, 84–98 (2018).
54. Sporre, M. K. et al. Large difference in aerosol radiative effects from BVOC-SOA treatment in three Earth system models. *Atmos. Chem. Phys.* **20**, 8953–8973 (2020).
55. Pacifico, F., Folberth, G. A., Jones, C. D., Harrison, S. P. & Collins, W. J. Sensitivity of biogenic isoprene emissions to past, present, and future environmental conditions and implications for atmospheric chemistry. *J. Geophys. Res. Atmos.* **117**, <https://doi.org/10.1029/2012JD018276> (2012).
56. Mulcahy, J. P. et al. Description and evaluation of aerosol in UKESM1 and HadGEM3-GC3.1 CMIP6 historical simulations. *Geosci. Model Dev.* **13**, 6383–6423 (2020).
57. Seland, Ø. et al. Overview of the Norwegian Earth System Model (NorESM2) and key climate response of CMIP6 DECK, historical, and scenario simulations. *Geosci. Model Dev.* **13**, 6165–6200 (2020).
58. Horowitz, L. W. et al. The GFDL global atmospheric chemistry-climate model AM4.1: model description and simulation characteristics. *J. Adv. Model. Earth Syst.* **12**, e2019MS002032 (2020).
59. Hodzic, A. et al. Rethinking the global secondary organic aerosol (SOA) budget: stronger production, faster removal, shorter lifetime. *Atmos. Chem. Phys.* **16**, 7917–7941 (2016).
60. Gettelman, A. et al. The whole atmosphere community climate model version 6 (WACCM6). *J. Geophys. Res. Atmos.* **124**, 12380–12403 (2019).
61. Carlton, A. G., Pinder, R. W., Bhave, P. V. & Pouliot, G. A. To what extent can biogenic SOA be controlled? *Environ. Sci. Technol.* **44**, 3376–3380 (2010).
62. Naik, V., Delire, C. & Wuebbles, D. J. Sensitivity of global biogenic isoprenoid emissions to climate variability and atmospheric CO₂. *J. Geophys. Res. Atmos.* **109** <https://onlinelibrary.wiley.com/doi/abs/10.1029/2003JD004236> eprint: <https://onlinelibrary.wiley.com/doi/pdf/10.1029/2003JD004236> (2004).
63. Wang, B., Shuman, J., Shugart, H. & Lerdau, M. Biodiversity matters in feedbacks between climate change and air quality: a study using an individual-based model. *Ecol. Appl.* **5**, 1223–1231 (2018).

64. Arora, V. K. et al. Carbon–concentration and carbon–climate feedbacks in CMIP6 models and their comparison to CMIP5 models. *Biogeosciences* **17**, 4173–4222 (2020).
65. Shrivastava, M. et al. Recent advances in understanding secondary organic aerosol: Implications for global climate forcing. *Rev. Geophys.* **55**, 509–559 (2017).
66. Hoesly, R. M. et al. Historical (1750–2014) anthropogenic emissions of reactive gases and aerosols from the Community Emissions Data System (CEDS). *Geosci. Model Dev.* **11**, 369–408 (2018).
67. Guenther, A. B. et al. The model of emissions of gases and aerosols from nature version 2.1 (MEGAN2.1): an extended and updated framework for modeling biogenic emissions. *Geosci. Model Dev.* **5**, 1471–1492 (2012).
68. Wilkinson, M. J. et al. Leaf isoprene emission rate as a function of atmospheric CO₂ concentration. *Glob. Chang. Biol.* **15**, 1189–1200 (2009).
69. Guenther, A. B., Zimmerman, P. R., Harley, P. C., Monson, R. K. & Fall, R. Isoprene and monoterpene emission rate variability: model evaluations and sensitivity analyses. *J. Geophys. Res. Atmos.* **98**, 12609–12617 (1993).
70. Fiore, A. M. et al. Global air quality and climate. *Chem. Soc. Rev.* **41**, 6663 (2012).
71. Turnock, S. T. et al. Historical and future changes in air pollutants from CMIP6 models. *Atmosp. Chem. Phys.* **20**, 14547–14579 (2020).

Acknowledgements

R.J. Allen is supported by NSF grant AGS-2153486. E.S. Thomson is supported by the Swedish Research Councils, FORMAS (2017-00564) and VR (2020-03497) and by the Swedish Strategic Research Area MERGE. S. Turnock would like to acknowledge that support for this work came from the UK-China Research and Innovation Partnership Fund through the Met Office Climate Science for Service Partnership (CSSP) China as part of the Newton Fund.

Author contributions

J.G. performed data analysis and wrote the paper. R.J.A. conceived the project, designed the study, performed analyses, and wrote the paper. S.T.T. performed UKESM1-0-LL simulations and provided additional data. L.W.H. and P.G. performed GFDL-ESM4 simulations and provided additional data. K.T. and S.E.B. performed GISS-E2-1-G

simulations. D.O. performed NorESM2-LM simulations. E.S.T. advised on methods. All authors discussed results and contributed to the writing of the manuscript.

Competing interests

The authors declare no competing interests.

Additional information

Supplementary information The online version contains supplementary material available at <https://doi.org/10.1038/s43247-023-00688-7>.

Correspondence and requests for materials should be addressed to Robert J. Allen.

Peer review information *Communications Earth & Environment* thanks Yangyang Xu and the other, anonymous, reviewer(s) for their contribution to the peer review of this work. Primary handling editors: Aliénor Lavergne. Peer reviewer reports are available.

Reprints and permission information is available at <http://www.nature.com/reprints>

Publisher's note Springer Nature remains neutral with regard to jurisdictional claims in published maps and institutional affiliations.



Open Access This article is licensed under a Creative Commons Attribution 4.0 International License, which permits use, sharing, adaptation, distribution and reproduction in any medium or format, as long as you give appropriate credit to the original author(s) and the source, provide a link to the Creative Commons license, and indicate if changes were made. The images or other third party material in this article are included in the article's Creative Commons license, unless indicated otherwise in a credit line to the material. If material is not included in the article's Creative Commons license and your intended use is not permitted by statutory regulation or exceeds the permitted use, you will need to obtain permission directly from the copyright holder. To view a copy of this license, visit <http://creativecommons.org/licenses/by/4.0/>.

© The Author(s) 2023